CHAPTER 5

EFFECT OF ULTRASONIC SHOT PEENING ON MICROSTRUCTURE, CORROSION RESISTANCE, BIOCOMPATIBILITY AND LOW CYCLE FATIGUE BEHAVIOR OF NICKEL-FREE AUSTENITIC STAINLESS STEEL (HNS)

5.1. Introduction

Nanostructured materials are considered for their enhanced mechanical, chemical and physical properties. Ultrasonic shot peening (USP) is a technique of modifying the surface of metallic materials; it refines the coarse-grained microstructure to the nanoscale, induces compressive residual stress and enhances wettability. These factors affect the properties of metallic materials. Electrochemical corrosion, biocompatibility and fatigue are surface sensitive properties and they strongly depend on the surface condition of materials. This chapter presents the influence of USP on microstructure, hardness, electrochemical corrosion in simulated body fluid (SBF), *in vitro* cell culture and proliferation and low cycle fatigue. Disc-shaped samples were prepared and subjected to USP for different durations of 0.5, 1 and 2 minutes, using 2 mm and 3 mm diameter shots and characterized for the refinement of microstructure, using X-ray diffraction and transmission electron microscope. The variation of microhardness and residual stress from the USPed surface towards the interior was also measured. Potentiodynamic polarization tests were performed on the different USPed samples in Ringer's solution and the results are compared with that of the non-treated (Un-USP) sample. Enhancement in breakdown potential was observed following the short duration of USP. In contrast, there was reduction in corrosion resistance for the longer duration of USP, which is discussed in detail. The *in vitro* cell culture and proliferation experiments

were conducted following the USP of the HNS and enhancement in cell proliferation was observed.

Low cycle fatigue (LCF) tests were conducted following USP in air at room temperature and the results are compared with that of the Un-USP samples. USP was carried out with 3 mm shots for a wide range of duration, from 3 minutes to 18 minutes on the HNS and the LCF life was evaluated at different total strain amplitudes ($\Delta\varepsilon_t/2$) of ± 0.40%, ± 0.50%, ± 0.60% and ± 0.80%. It was observed that the cyclic life of the HNS was strongly dependent on both the process parameter, the duration of USP as well as the LCF test parameter ($\Delta\varepsilon_t/2$). LCF life increased with the duration of USP at lower strain amplitudes, whereas it decreased at higher strain amplitudes.

5.2. Surface Morphology and Surface Roughness

Surface morphology of the different USPed samples is shown in **Fig. 5.1.**

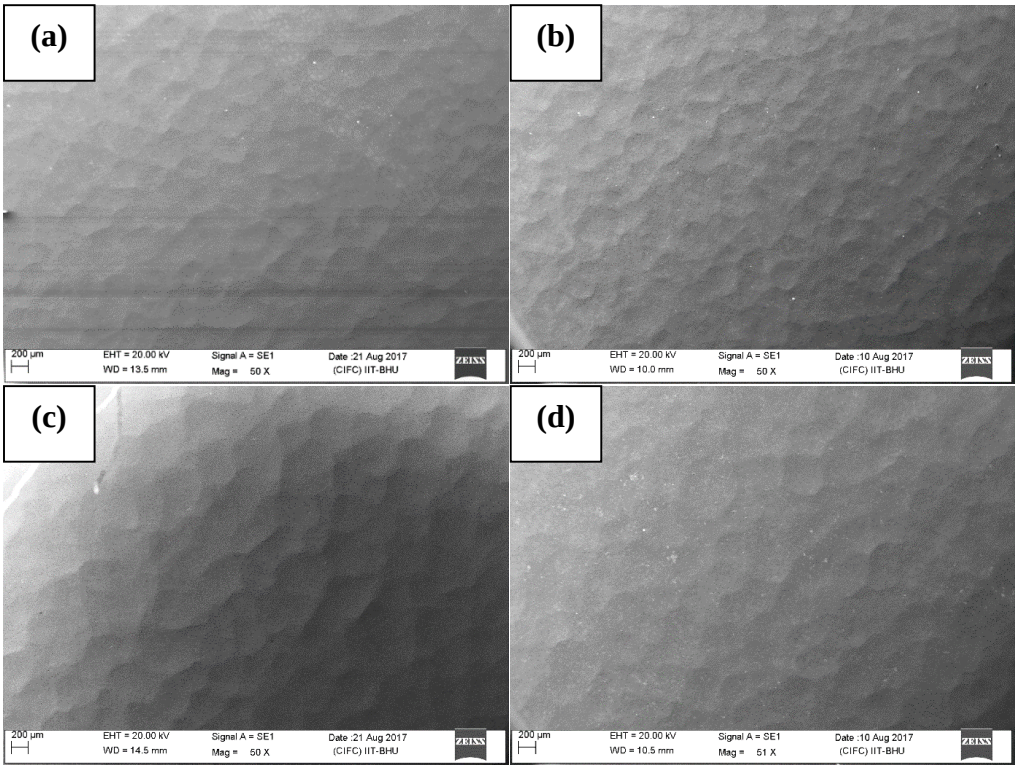

Fig. 5.1. Surface morphology of the HNS in various USPed conditions: (a) USP 2-0.5, (b) USP 2-2, (c) USP 3-0.5, and (d) USP 3-2.

Surface features like shallow dimples may be seen following the USP. The size of the dents (shallow dimples) was noticeably increased with the size of shots and decreased with USP duration. They are also examined at higher magnification and surface topography of the different USPed samples is shown in **Fig. 5.2**.

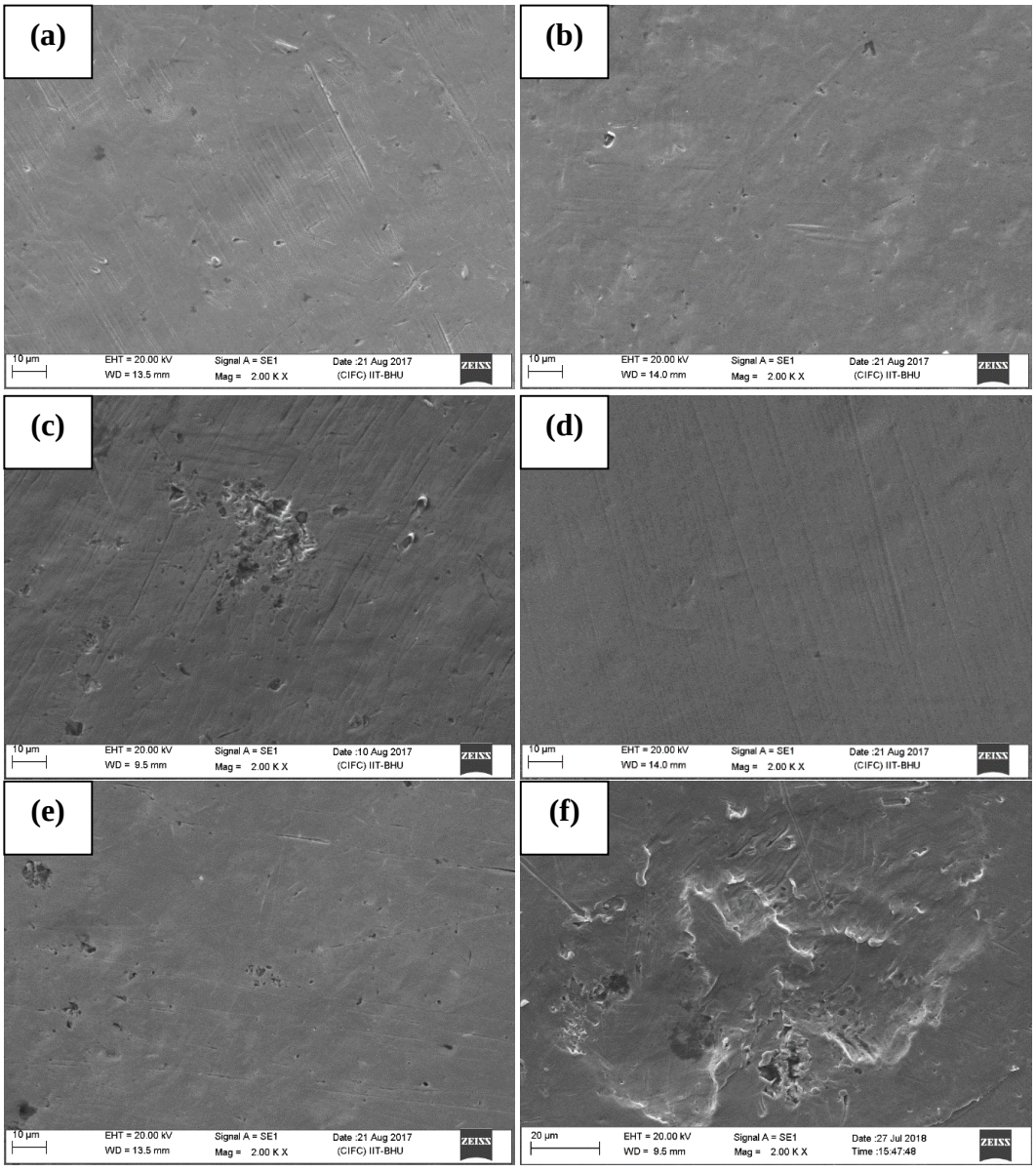

Fig. 5.2. Surface morphology of the samples of HNS in different conditions of USP: (a) USP 2-0.5, (b) USP 2-1, (c) USP 2-2, (d) USP 3-0.5, (e) USP 3-1, and (f) USP 3-2.

Increase in surface damage with duration of USP is evident. The USP 2-0.5 and USP 3-0.5 samples show similar surface morphology without significant damage, whereas

surface of the other samples is notably damaged due to the excessive USP. Surface damage is more for the USP 3-1 than USP 2-1 and USP 3-2 is most damaged.

The various surface roughness parameters of disc-shaped samples used for corrosion study, under different USPed conditions, were measured and are presented in **Table 5.1.** Initially, the average surface roughness (Ra) increased significantly following USP; the surface roughness increased with the size of shots. The total height of the roughness profile was maximum for the USP 2-1 and USP 3-2 specimens. Initially, after 30 s of USP, there is a significant increase in the roughness, but after 1 min of USP, there is a slight increase in the roughness compared to 30 s. However, the roughness of the samples USPed for 2 min decreased and was less than that of the sample USPed for 30 s. This trend was observed for the both sizes of the shots.

Table 5.1. Surface roughness parameters of flat disc-shaped samples of the HNS in different conditions of USP.

USP condition	R_a (µm)	R_z (µm)	R_t (µm)
Un-USP	0.026 ± 0.006	0.197 ± 0.047	0.356 ± 0.134
USP 2-0.5	1.37 ± 0.05	6.11 ± 0.26	9.24 ± 0.83
USP 2-1	1.47 ± 0.08	7.19 ± 0.30	11.27 ± 0.93
USP 2-2	1.30 ± 0.06	6.18 ± 0.53	7.74 ± 1.23
USP 3-0.5	1.49 ± 0.06	7.57 ± 0.64	10.35 ± 0.94
USP 3-1	1.54 ± 0.09	6.59 ± 0.33	8.09 ± 1.29
USP 3-2	1.29 ± 0.06	6.06 ± 0.29	11.27 ± 0.92

Surface roughness was also measured over the gauge section of the fatigue test samples in different conditions and their values corresponding to varying durations of USP are presented in **Table 5.2**. The average surface roughness increased considerably with the duration of USP from 3 to 6 minutes, and after that, it decreased. However, the total height of roughness profile and roughness depth remained unaffected by the USP duration.

Table 5.2. Surface roughness parameters over gauge section of the LCF samples in different conditions of USP.

USP condition	R_a (µm)	R_z (µm)	R_t (µm)
Un-USP	0.015 ± 0.004	0.121 ± 0.037	0.218 ± 0.154
USP 3-3	1.69 ± 0.09	7.74 ± 0.9	10.51 ± 0.92
USP 3-6	1.79 ± 0.07	7.21 ± 0.35	10.57 ± 1.03
USP 3-10	1.40 ± 0.08	6.57 ± 0.8	10.03 ± 1.17
USP 3-14	1.55 ± 0.07	6.76 ± 0.79	9.17 ± 0.96
USP 3-18	1.36 ± 0.19	6.355 ± 0.23	9.18 ± 0.99

Note: R_a: Arithmetic mean deviation of the roughness profile, R_z: Mean roughness depth, R_t: Total height of roughness profile.

5.3. Microstructure Characterization of the USPed Samples

The modification of microstructure in the longitudinal section, normal to USPed surface, of the USPed samples, is shown in **Fig. 5.3**. A large number of deformation bands, identified as deformation twins of various orientations and their extensive intersection, in the USPed specimens, may be seen from the SEM micrographs. Mechanical twins resulting from USP have been previously reported in 304L [169]. Multidirectional twins were observed near the surface. There was a subtle change from the multidirectional twins to single directional twins from the USPed surface towards the interior and a gradient net-like microstructure was developed. The multidirectional twins diminished with increase in the depth from the USPed surface and their depth varied with the duration and shot diameter used for the USP. There was an increase in the depth of the modified microstructure, termed as USP affected layer, with increase in the duration of USP and shot size. The USP affected layer, estimated from the SEM micrographs, is found up to the depth of ~ 140 µm, 150 µm, 260 µm and 300 µm for the USP 2-1, USP 3-1, USP 3-3, and USP 3-6 samples, respectively.

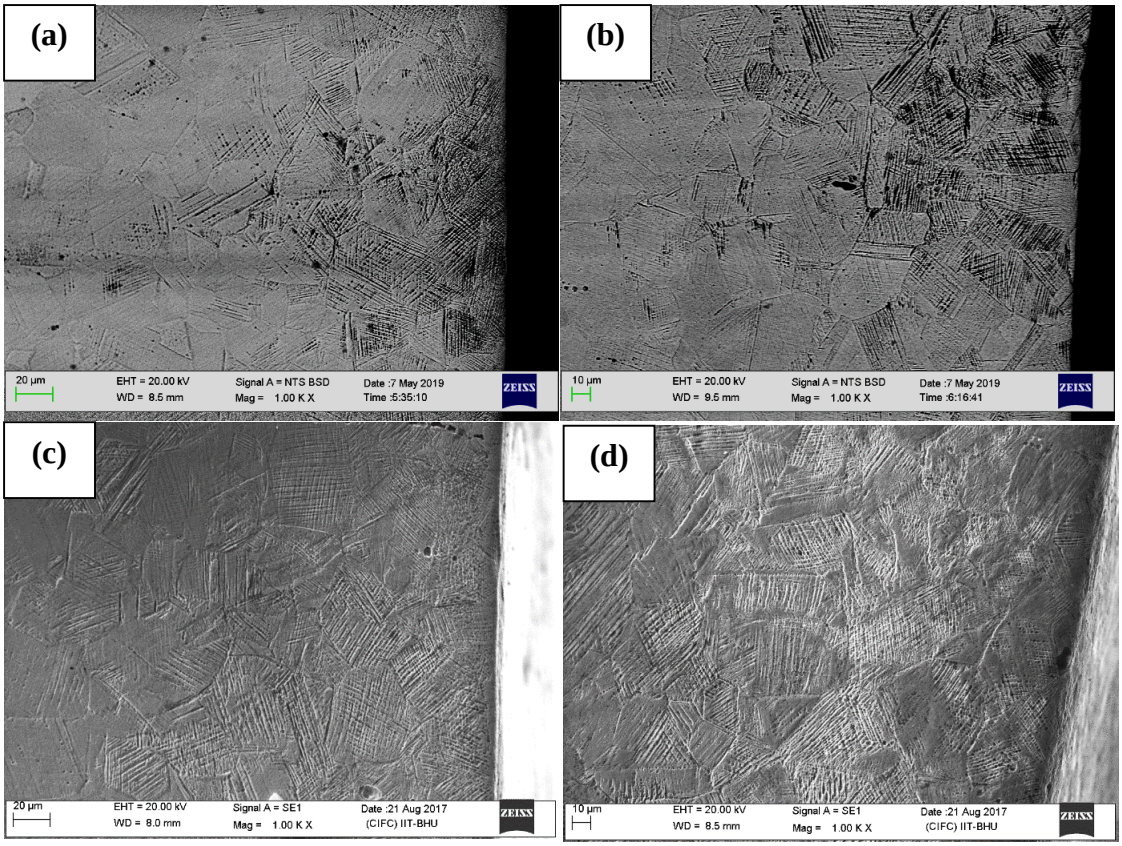

Fig. 5.3. SEM micrographs of the longitudinal sections, normal to the USPed flat surface of the disc-shaped samples, in various USPed conditions: (a) USP 2-1, (b) USP 3-1, (c) USP 3-3, and (d) USP 3-6. The right side edge is the edge of the USPed surface.

X-ray diffractograms of the Un-USP sample, and those with varying USP, are shown in **Fig. 5.4a**. A magnified view of the peaks of the plane (111) is displayed in **Fig. 5.4b**. There are no additional peaks for the samples subjected to USP, apart from the existing peaks of the austenite. However, there is peak broadening and a peak shift towards the higher angle, following the USP.

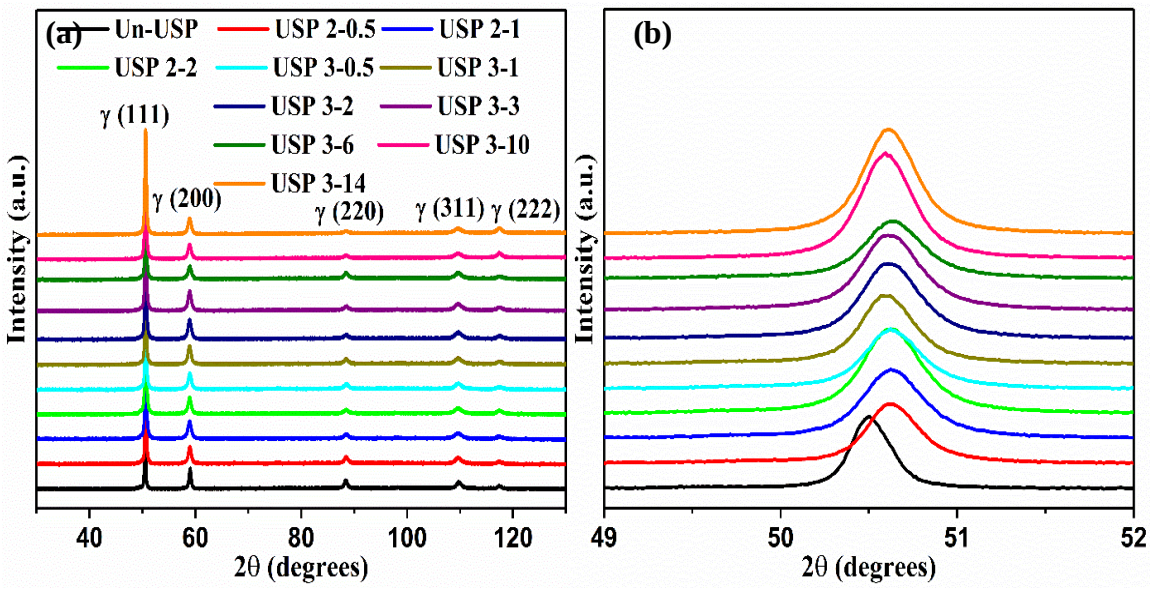

Fig. 5.4. X-ray diffraction patterns of the HNS in the Un-USP and different USPed conditions: (a) X-ray diffractograms, and (b) magnified (111) peaks.

The crystallite size and microstrain in the USPed samples were determined by XRD peak analysis, using Scherrer-Wilson [186] and Williamson-Hall relationships [187] expressed in the **Eqs. 5.1 and 5.2**, respectively and the respective values are given in **Table 5.3**.

$$D = \frac{0.9\lambda}{B\cos\theta} \tag{5.1}$$

$$B\cos\theta = \frac{0.9\,\lambda}{D} + 4\varepsilon\sin\theta \tag{5.2}$$

Where, D is average crystallite size, λ is X-ray wavelength, B is line broadening, θ is Bragg angle and ε is microstrain. There is a gradual decrease in the crystallite size with increase in the USP duration and shot size. The mean microstrain increased following USP; however, there is no systematic variation.

Table 5.3. Crystallite size and microstrain of the USPed HNS samples, estimated by XRD analysis.

USP condition	Average crystallite size (nm)	Mean microstrain (%)
USP 2-0.5	22 ± 7	0.22 ± 0.006
USP 2-1	21 ± 4	0.22 ± 0.004
USP 2-2	18 ± 7	0.19 ± 0.005
USP 3-0.5	20 ± 8	0.20 ± 0.005
USP 3-1	17 ± 3	0.22 ± 0.004
USP 3-2	15 ± 4	0.22 ± 0.004
USP 3-3	15 ± 2	0.41 ± 0.09
USP 3-6	14 ± 2	0.42 ± 0.10
USP 3-10	13 ± 3	0.43 ± 0.14
USP 3-14	12 ± 2	0.41 ± 0.10

The microstructure of the USPed samples was also examined by TEM. The TEM micrographs and the corresponding selected area diffraction (SAD) patterns are shown in **Figs. 5.5 and 5.6**. Nanosize grains and subgrains may be seen near the USPed surface. Concentric rings may be observed in the SAD patterns from the top surfaces of the USP 2-2, USP 3-0.5, USP 3-3 and USP 3-6 samples, strengthening the presence of nanograins with random crystallographic orientation. Deformation twins of ~ 10 nm lamellar thickness were observed at a depth of ~ 20 μm from the USPed surface (**Fig. 5.6**). The corresponding diffraction pattern was indexed as FCC system. The twins were formed in two different orientations and intersected each other at ~ 72.5º. The twins in one specific orientation are parallel to each other. A high dislocation density was also observed inside the grains. The contrast within the grains is not uniform due to the high level of internal stresses and elastic distortion in the crystal lattice. These observations are in line with those of Zhang et al. in 304L stainless steel [169].

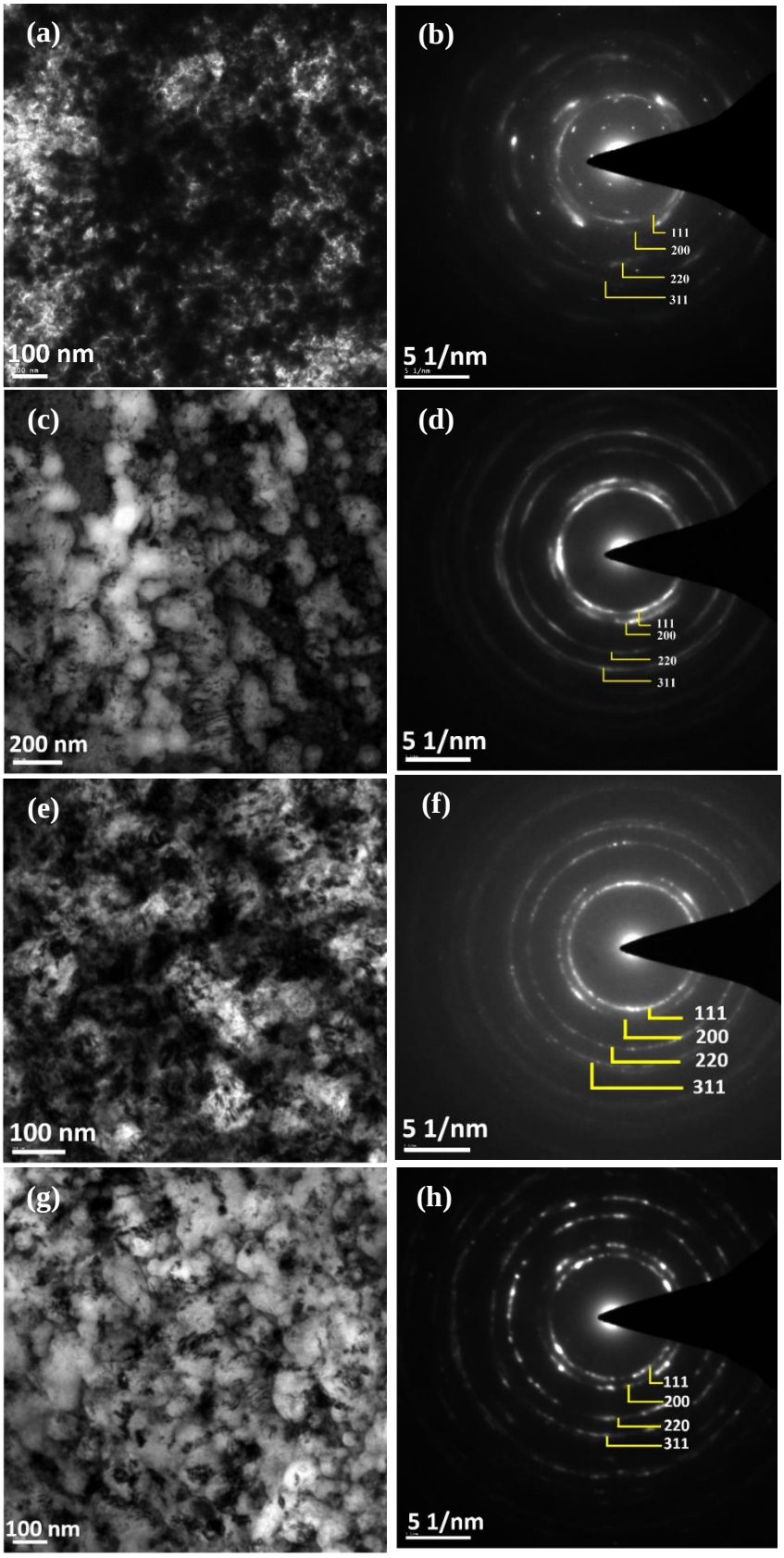

Fig. 5.5. Bright field TEM micrographs and their corresponding SAD patterns from the top surface regions of the HNS in different USPed conditions: (a, b) USP 2-2; (c, d) USP 3-0.5; (e, f) USP 3-3; and (g, h) USP 3-6.

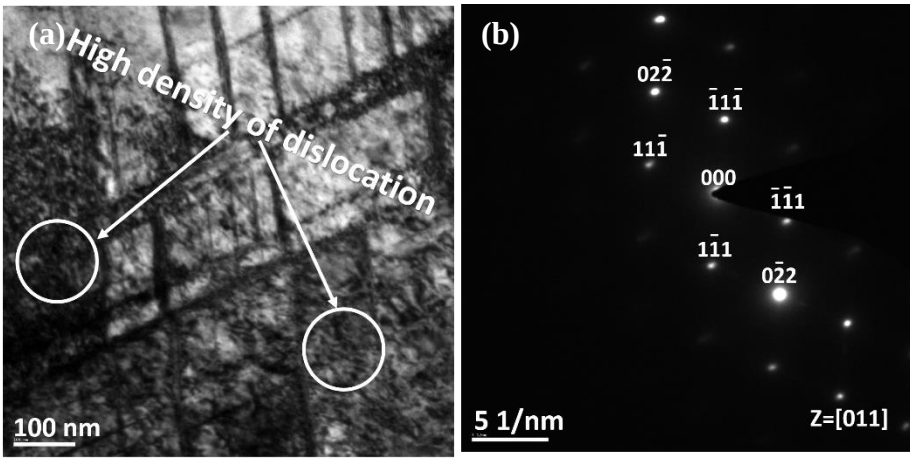

Fig. 5.6. (a) Bright field TEM micrograph and (b) corresponding SAD patterns of the USP 3-6 sample at the depth of ~ 20 µm from the USPed surface.

5.4. Hardness and Residual Stress

The effect of the USP on hardness in the surface region is presented in **Fig. 5.7**.

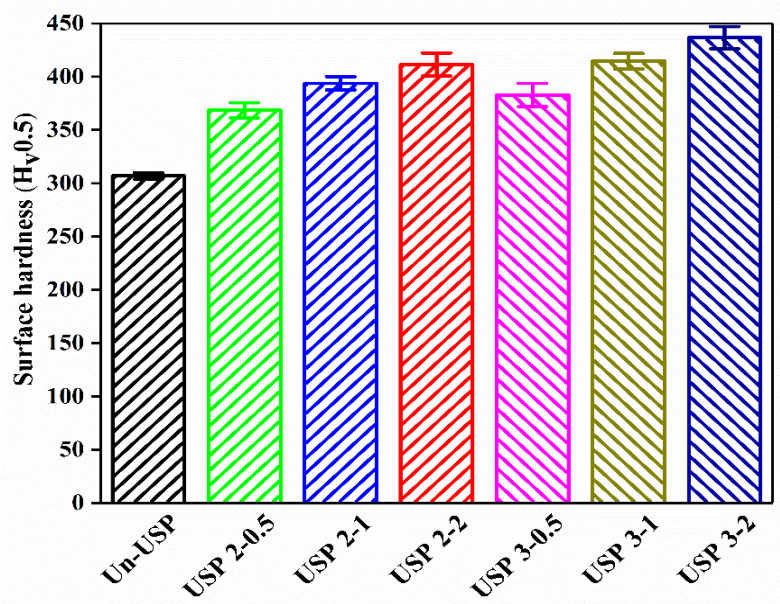

Fig. 5.7. Surface hardness of the HNS in different USPed conditions.

There was a gradual increase in hardness with the duration of USP for both sizes of the shots. The increase in surface hardness was 20 % and 28 % following USP for the duration 0.5 and 1 min, respectively with 2 mm shots. However, the increase in surface hardness was higher for the specimens shot-peened with 3 mm shots than that shot-

peened with 2 mm shots for the same duration of USP. The increase in surface hardness was 25 %, 35 % and 42 % following USP for the duration 0.5 min, 1 min and 2 min, respectively, with 3 mm shots.

The variation of microhardness in the USPed samples was measured on the longitudinal section of the disc-shaped samples, perpendicular to the USPed surface along the diameter, from the surface to the interior. The microhardness profiles of the samples USPed for different conditions are shown in **Fig. 5.8**.

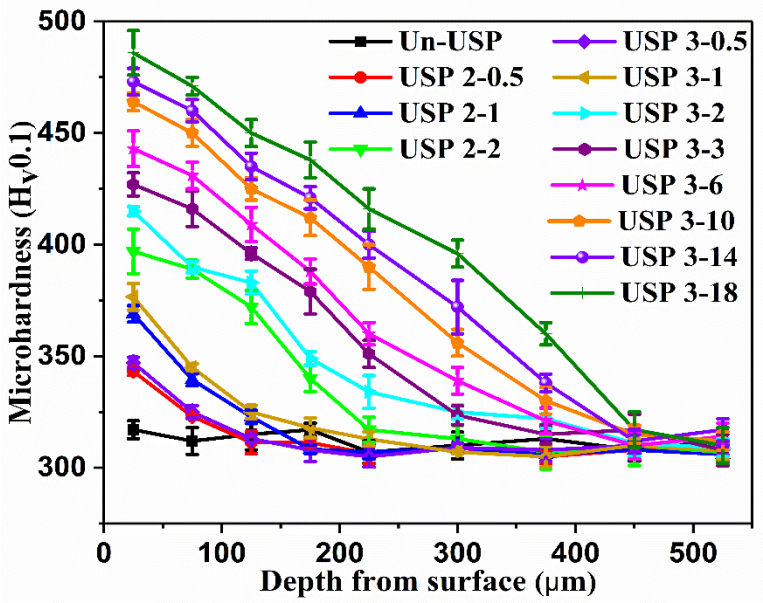

Fig. 5.8. Microhardness profiles of the HNS in different USPed conditions.

It is evident that the microhardness of the USPed samples increased appreciably close to the USPed edge. There was a gradual decrease in hardness with increasing depth from the USPed surface due to the gradient microstructure from the USPed surface towards the interior. There was decrease in the multidirectional twins with increase in the depth from the surface. The depth up to which the microhardness varies is more for the specimens USPed with the bigger shots of 3 mm diameter. The level of microhardness progressively increased with the duration of USP.

The residual stress in USPed samples was also measured. The stresses induced on the USPed surface as well as up to a certain depth were measured. The residual stress measured on the USPed surface was -227 MPa and -301 MPa for the USP 2-1 and USP 3-1 samples, respectively. The residual stress variation with depth in the USPed samples is shown in **Fig. 5.9**.

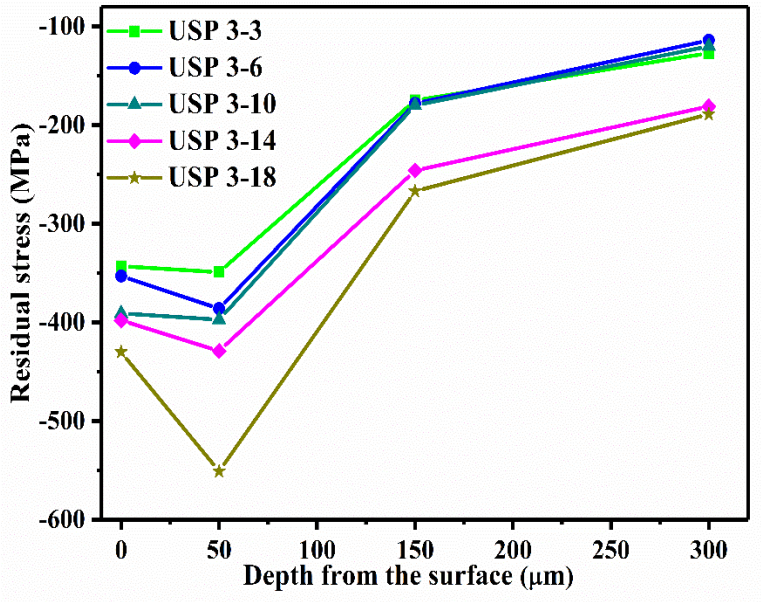

Fig. 5.9. Variation of residual stress induced in the HNS in different USPed conditions from the surface to 300 µm depth.

The residual stress is compressive and its magnitude increases with the duration of USP. The maximum value of the compressive residual stress was found in the sub-surface region. For the USP 3-18 sample, residual stress was -430 MPa at the USPed surface and -551 MPa at a depth of 50 µm from the surface. It decreased to -189 MPa at 300 µm below the surface.

5.5. Effect of Ultrasonic Shot Peening on Corrosion Resistance of the HNS

Electrochemical corrosion of the HNS in various USPed conditions was studied in Ringer's solution by potentiodynamic polarization and was compared with that of the Un-USP sample. The polarization curves of the Un-USP and different USPed specimens

are displayed in **Fig. 5.10**. The E_{corr} (corrosion potential), i_{corr} (corrosion current density) and E_{bd} (breakdown potential) of the samples were evaluated from the respective sample's polarization curve. The i_{corr} was determined from the intersection of an extrapolated linear portion of the cathodic curve with a horizontal line of the open circuit potential (OCP).

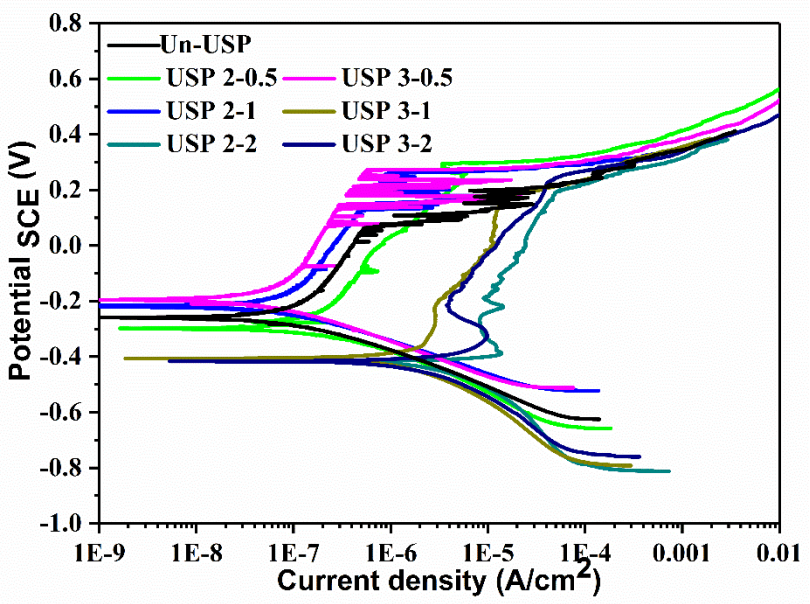

Fig. 5.10. Potentiodynamic polarization plots of the HNS in the Un-USP and different USPed conditions.

The corrosion parameters measured from potentiodynamic polarisation in the Un-USP and different USPed conditions are presented in **Table 5.4**. It may be seen that corrosion potential of the USP 2-0.5, USP 2-2, USP 3-1 and USP 3-2 samples is negative, whereas it is positive for the USP 2-1 and USP 3-0.5 samples, with respect to that of the Un-USP sample. The E_{corr} is maximum for the USP 3-0.5 sample. Corrosion current density (i_{corr}) of the USP 2-2, USP 3-1 and USP 3-2 samples are appreciably higher than that of the Un-USP. The passive current density of the USP 2-0.5, USP 2-1 and USP 3-0.5 samples is comparable to that of the Un-USP, whereas it is higher for the other conditions (**Table 5.4**). It is evident from the polarization curves in **Fig. 5.10** that the dissolution rate of

material in the passive region is lower for the USP 2-1 and USP 3-0.5 samples than that of the Un-USP sample. The USP 2-0.5, USP 2-1 and USP 3-0.5 samples display comparable breakdown potential (E_{bd}). It may be seen that USP 2-1 and USP 3-0.5 conditions of USP are best suited from the point of view of the resistance of the material against corrosion in the SBF environment.

Table 5.4. Corrosion parameters of the HNS in different conditions.

Material Designation	**Corrosion potential, E_{corr} (mV_{SCE})**	**Breakdown potential, E_{bd} (mV_{SCE})**	**Corrosion current density, i_{corr} ($\mu A/cm^2$)**	**Passive current density at 0 mV, i_p ($\mu A/cm^2$)**
UN-USP	-260	196	0.13	0.40
USP 3-0.5	-197	262	0.06	0.17
USP 3-1	-405	173	1.62	11.20
USP 3-2	-418	232	3.01	12.08
USP 2-0.5	-300	290	0.20	0.78
USP 2-1	-216	260	0.08	0.25
USP 2-2	-413	197	6.05	25.1

Thus, a longer duration of USP reduces the resistance of the HNS against corrosion in the SBF environment. In the USP 3-0.5 sample, corrosion current density is minimum, whereas corrosion potential is found to be maximum.

5.6. Effect of Ultrasonic Shot Peening on Cell Culture and Proliferation of the HNS

The *in vitro* cell culture and proliferation were examined on HNS samples following USP. The fluorescent microscopic images of the MG-63 human bone osteosarcoma cells cultured on the various samples are shown in **Fig. 5.11**.

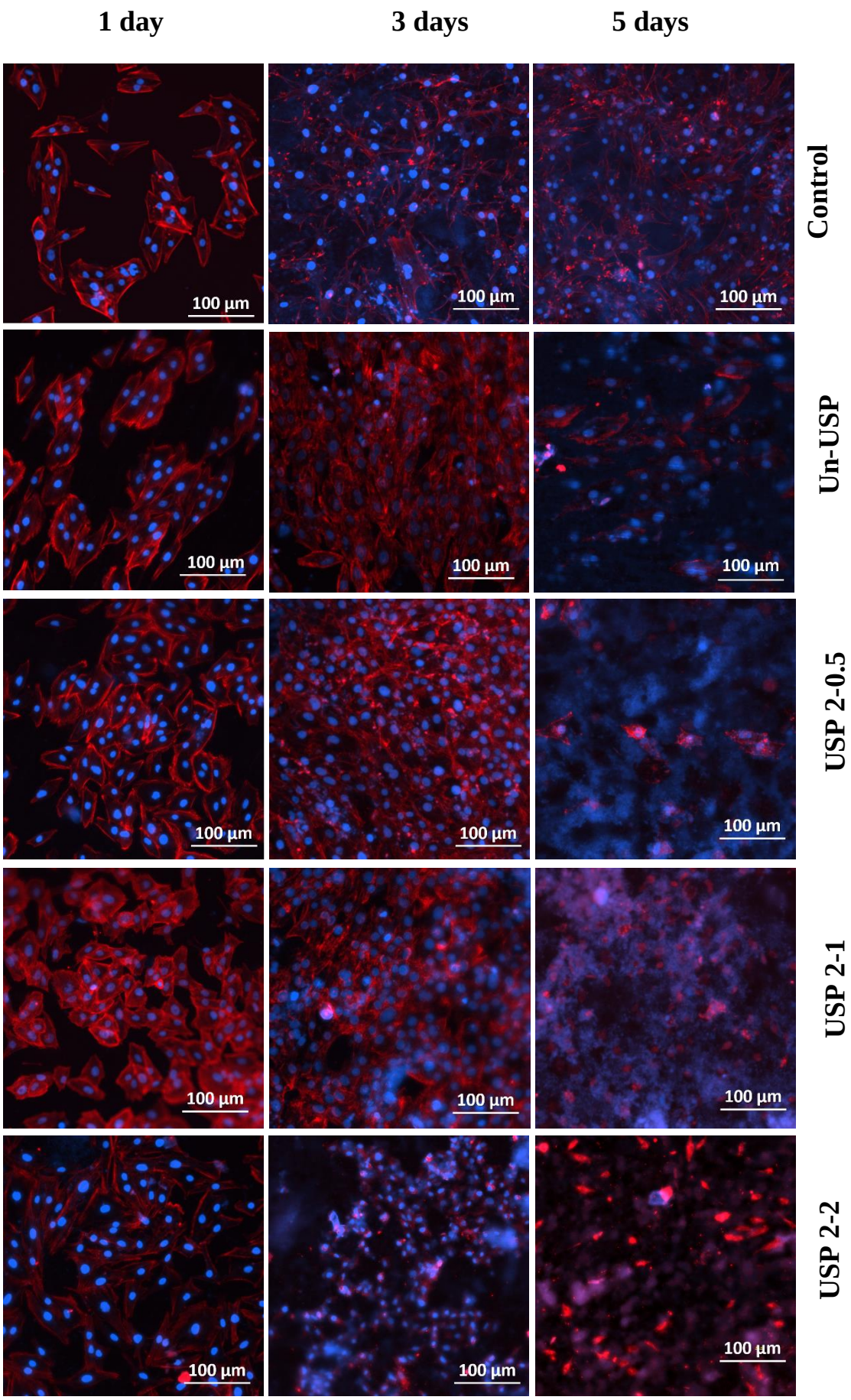
1 day
3 days
5 days
Control
Un-USP
USP 2-0.5
USP 2-1
USP 2-2
100 µm

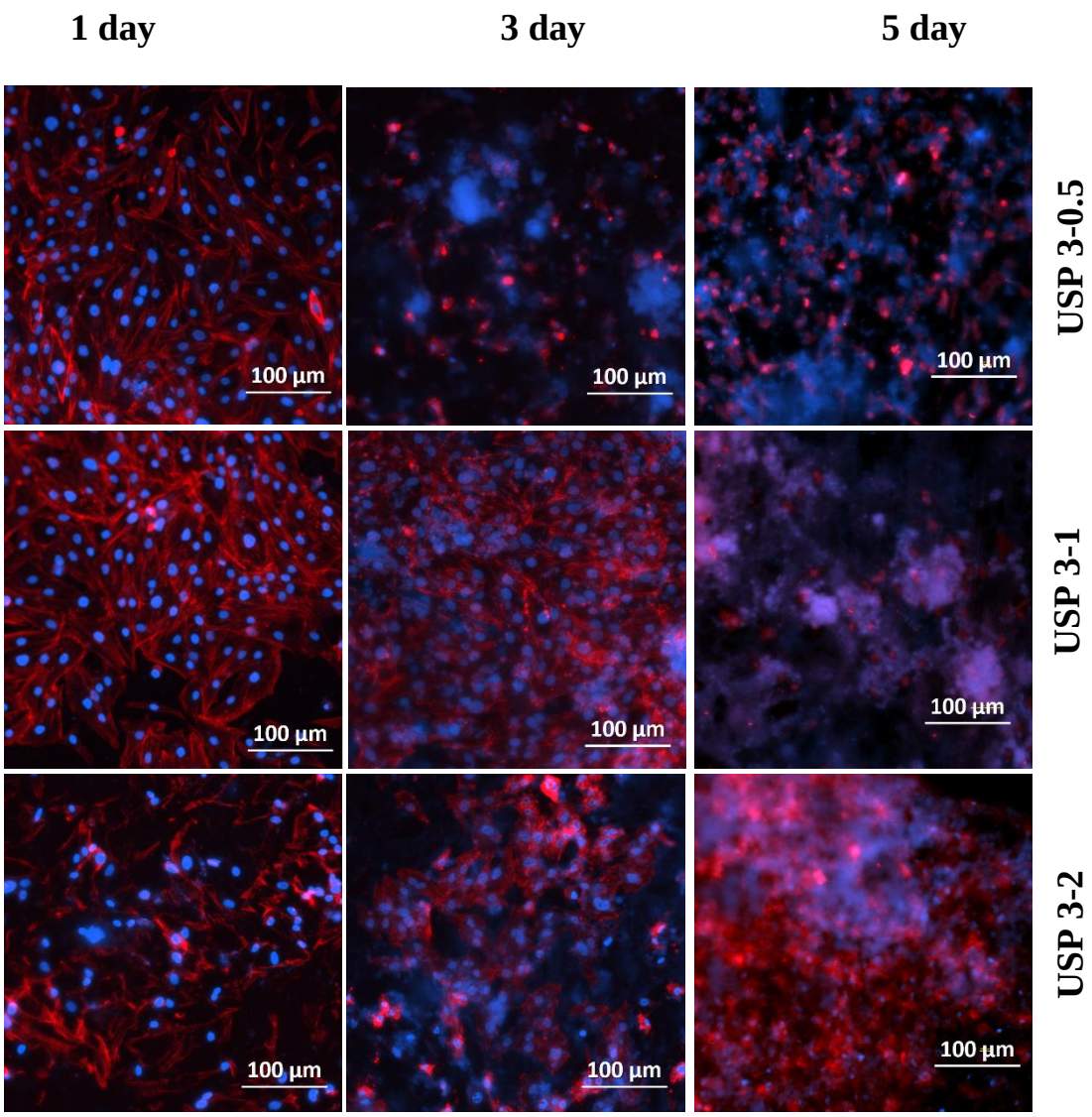

Fig. 5.11. Panel representing the fluorescent cell culture images of MG-63 human bone osteosarcoma cells on the various HNS samples; after 1 day, 3 days and 5 days of incubation. Blue color: nuclei staining; red color: actin cytoskeleton filaments staining.

There is an appreciable increase in the cell coverage with an increase in the culture time on all the samples, showing a gradual cellular growth with time. The USPed samples show comparatively higher cell coverage on the surface with respect to the Un-USP sample, indicating a more increased rate of spreading of cells over the USPed samples than the Un-USP. However, there is a negligible effect of the size of shots on the cell spreading.

The cell proliferation of MG-63 osteoblast-like cells in different USPed conditions was studied by MTT assay and is shown in **Fig. 5.12.**

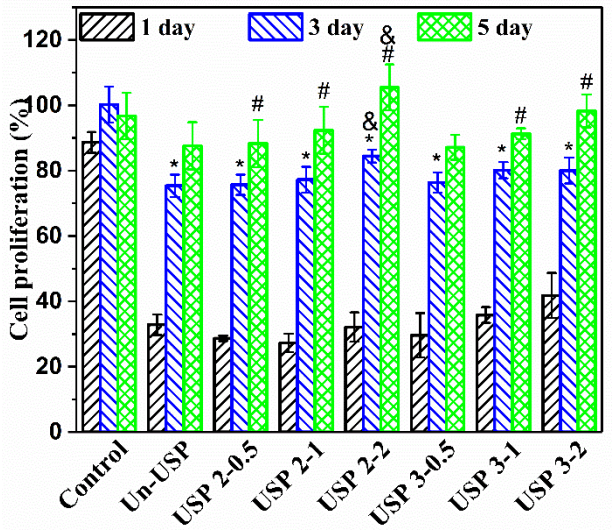

Fig. 5.12. Histograms representing comparison of MG-63 cell proliferation after 1, 3 and 5 days of incubation by MTT assay for the HNS in various USPed conditions. In this experiment, absorbance of control for the 5th day culture was taken as reference for all the samples. $^{*}p \leq 0.05$ with respect to 1 day of corresponding group. $^{\#}p \leq 0.05$ with respect to 3 days of corresponding group. $^{\&}p \leq 0.05$ with respect to Un-USP for the same day.

The mean percent cell proliferation of the MG-63 cells on the Un-USP shows that it increased from ~ 33% to 75% and 88% with increase in the duration of incubation from 1 day to 3 days and 5 days, respectively. The proliferation of the MG-63 cells on the USPed samples is found to increase significantly with the duration of incubation. The statistical analysis shows that the difference in the levels of cell proliferation for the different time points is significant at the level of 0.05. The mean percent cell proliferation of the USP 2-2 sample shows that it increased from ~ 33% to 84% and 105% with increase in the duration of incubation from 1 day to 3 days and 5 days, respectively, whereas for the USP 3-2 condition it increased from 41% to 80% to 98% with increase in the duration of incubation from 1 day to 3 days and 5 days, respectively. However, a

significant difference was observed between the various groups after different incubation times only for the USP 2-2 condition with respect to the Un-USP.

5.7. Effect of Ultrasonic Shot Peening on Low Cycle Fatigue Behavior of the HNS

Implants experience cyclic loading during service and may fail due to fatigue. In addition to the use of HNS for implants, it is also used in several other structural applications. There is dynamic loading and the components fail due to fatigue. USP was carried out on the HNS samples with 3 mm shots for a wide range of durations, from 3 to 18 min and its effect on low cycle fatigue (LCF) life was investigated.

5.7.1. Effect of Ultrasonic Shot Peening on Cyclic Stress Response

The variation of the cyclic stress amplitude ($\Delta\sigma/2$) with the number of cycles at varying total strain amplitudes ($\Delta\varepsilon_t/2$) for the different conditions is displayed in **Fig. 5.13**. The levels of the cyclic stress amplitude curves of the USPed samples are higher than the Un-USP at the respective strain amplitudes. There is also a cyclic hardening at all the $\Delta\varepsilon_t/2$ from ± 0.40 % to ± 0.80 % during the few initial cycles, followed by cyclic softening to the point of failure **(Figs. 5.13 b–e)**.

Fig. 5.14 shows the difference in the magnitudes of the cyclic tensile stress and cyclic compressive stress ($|\sigma_t|-|\sigma_c|$) as this varies with the number of cycles. A significant difference may be seen in the variation of $|\sigma_t|-|\sigma_c|$ of the Un-USP and USPed samples at the lowest $\Delta\varepsilon_t/2 = \pm 0.40$ %. In the USPed condition, $|\sigma_t|-|\sigma_c|$ is negative **(Fig. 5.14a)**, showing that the cyclic compressive stress is higher than the cyclic tensile stress, and it remains negative until the point of failure. In contrast, in the Un-USP condition, the negative difference between $|\sigma_t|$ and $|\sigma_c|$ decreases with an increase in the number of cycles and it becomes positive after ~ 5000 cycles. At $\Delta\varepsilon_t/2 = \pm 0.80$ % **(Fig. 5.14b)**,

there is a significant difference in $|\sigma_t|$-$|\sigma_c|$ between the Un-USP and USPed conditions for the initial two cycles, after which $|\sigma_t|$-$|\sigma_c|$ remains stable.

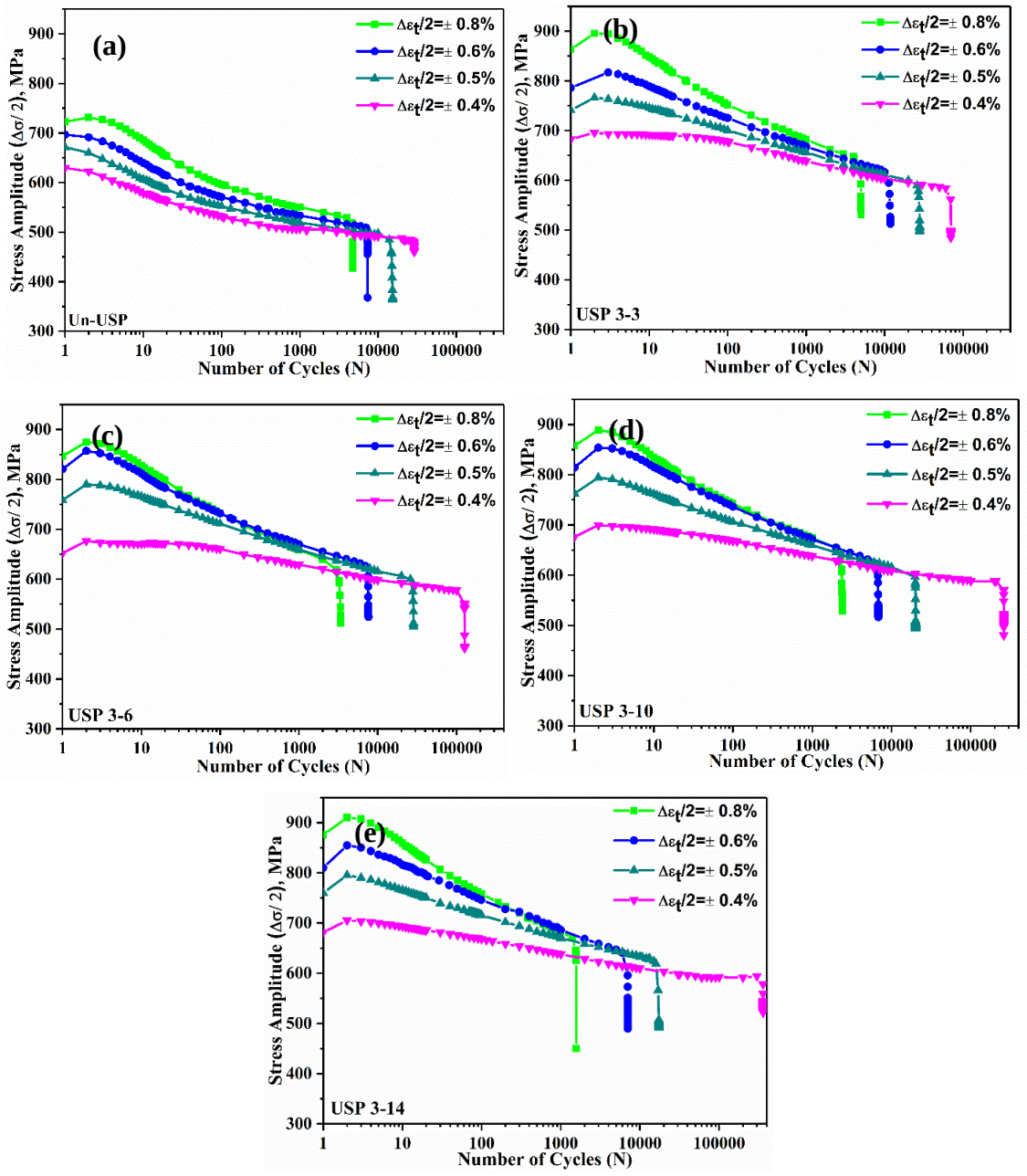

Fig. 5.13. Cyclic stress response curves of the HNS in different USPed conditions at varying strain amplitudes; (a) Un-USP, (b) USP 3-3, (c) USP 3-6, (d) USP 3-10, and (e) USP 3-14.

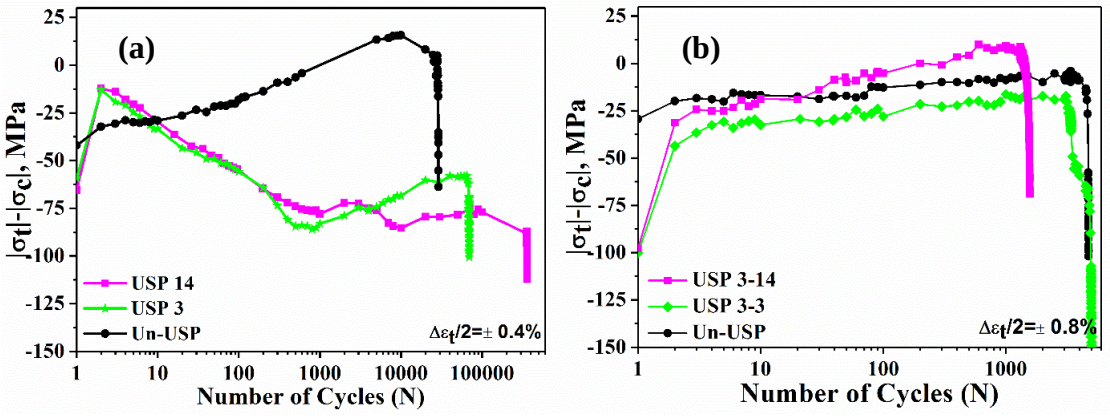

Fig. 5.14. Variation of $|\sigma_t|-|\sigma_c|$ with number of cycles at the different total strain amplitudes ($\Delta\varepsilon_t/2$): (a) ± 0.40 %, and (b) ± 0.80 %.

5.7.2. Effect of Ultrasonic Shot Peening on Low Cycle Fatigue Life

The data of the strain-controlled fatigue tests of the Un-USP sample, and those with varying USP, are presented in **Table 5.5**. The USP progressively increases the number of cycles endured before failure at the lower strain amplitudes ($\Delta\varepsilon_t/2 \leq \pm 0.50$ %). The effect of the lowest and highest strain amplitudes on the increase and decrease in fatigue life, with USP duration, is shown in **Fig. 5.15a**. At the lowest strain amplitude of ± 0.40 %, the fatigue life increases progressively with the duration of USP. It increases by ~ 11.5 times, following 14 minutes of USP and ~ 18 times from 18 minutes of USP. At $\Delta\varepsilon_t/2 = \pm 0.80$ %, the fatigue life is reduced by 67%, following 14 min of USP, implying a decrease in the beneficial effect of the USP with increasing $\Delta\varepsilon_t/2$. The fatigue life is analyzed using the Coffin-Manson relationship, shown in **Eq. 3.1.** The dependence of the number of reversals to failure ($2N_f$) on $\Delta\varepsilon_p/2$ for the different conditions is shown in **Fig. 5.15b**. The parameters ε'_f and c were evaluated from the plots of $\Delta\varepsilon_p/2$ vs. $2N_f$ and their values are presented in **Table 5.6**. Following the USP, there was a decrease in ε'_f, and an increase in c.

Table 5.5. LCF data of the Un-USP and USPed samples of HNS.

Material condition	Total strain amplitude ($\pm\Delta\varepsilon_t/2$) (%)	Elastic strain amplitude ($\pm\Delta\varepsilon_e/2$) (%) at $N_f/2$	Plastic strain amplitude ($\pm\Delta\varepsilon_p/2$) (%) at $N_f/2$	Fatigue life (N_f) Cycles
Un-USP	0.40	0.26	0.14	28927
	0.50	0.27	0.23	15389
	0.60	0.27	0.33	7330
	0.80	0.28	0.52	4760
USP 3	0.40	0.31	0.09	69835
	0.50	0.34	0.16	28069
	0.60	0.35	0.25	11834
	0.80	0.35	0.45	5021
USP 6	0.40	0.31	0.09	126815
	0.50	0.34	0.16	28518
	0.60	0.34	0.26	7629
	0.80	0.36	0.44	3402
USP 10	0.40	0.32	0.08	261581
	0.50	0.33	0.17	20199
	0.60	0.34	0.26	6841
	0.80	0.36	0.44	2400
USP 14	0.40	0.32	0.08	359364
	0.50	0.34	0.16	17364
	0.60	0.39	0.21	7038
	0.80	0.37	0.43	1574
USP 18	0.40	0.32	0.08	540480

Note: N_f: Fatigue life, $N_f/2$**:** Half-fatigue life

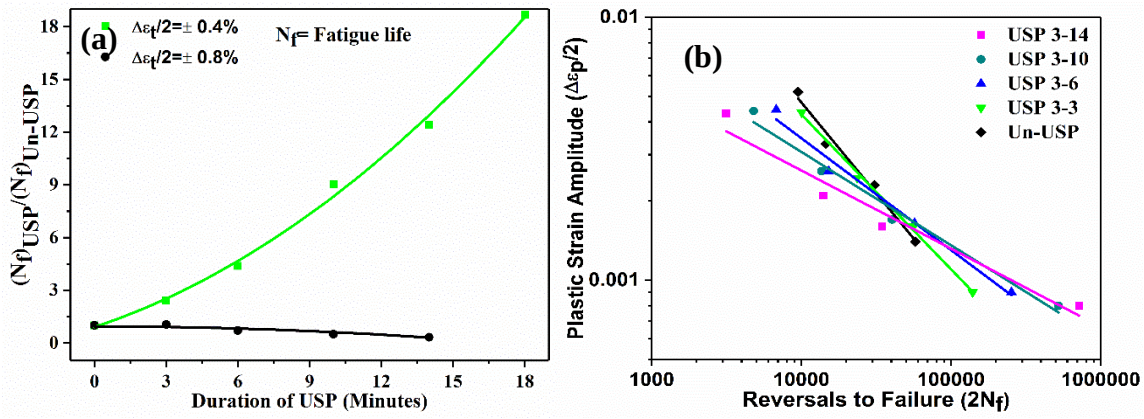

Fig. 5.15. (a) Effect of USP duration on fatigue life of the USPed samples with respect to Un-USP sample at high (± 0.80 %) and low (± 0.40 %) strain amplitudes, and (b) Coffin-Manson plots showing the variation of the number of reversals to failure ($2N_f$) with plastic strain amplitude for the Un-USP and different USPed conditions.

Table 5.6. LCF Parameters based on the strain-life relationship.

Samples	ε'_f	c
Un-USP	2.728	-0.689
USP 3	1.094	-0.599
USP 6	0.169	-0.423
USP 10	0.081	-0.355
USP 14	0.048	-0.309

5.7.3. Variation in the Cycles for Crack Initiation and Propagation

The number of cycles for crack initiation (N_i) was determined by the quotient curve [188]. The quotient curve was plotted between the ratio of the absolute values of compressive to tensile stress $|(\sigma_c/\sigma_t)|$ multiplied by 100, with the number of cycles (**Fig. 5.16a**). The major part of this curve is a plateau; however, it rises abruptly later (**Fig. 5.16a**). A straight line was fitted in the plateau region and a line was drawn parallel to this straight line at a 3% higher level than that of the fitted line. The number of cycles corresponding to the intersection of a 3% higher level parallel line with the quotient curve was taken as the number of cycles for crack initiation (N_i). The number of cycles for

crack propagation (N_p) was estimated from the difference between the total number of cycles to failure and crack initiation (N_f-N_i).

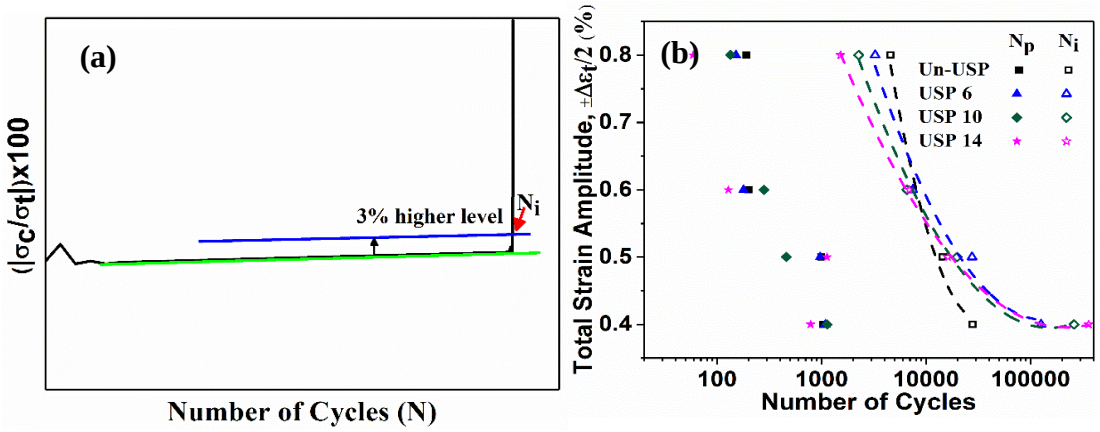

Fig. 5.16. (a) Schematic presentation of quotient plots ($|(\sigma_c/\sigma_t)|$ x 100), with number of cycles and determination of the number of cycles to crack initiation (N_i), (b) Variation of the number of cycles for crack initiation (N_i) and crack propagation (N_p), with % total strain amplitude ($\pm\Delta\varepsilon_t/2$) for the Un-USP and different USPed conditions.

Fig. 5.16b shows the variation of N_p and N_i with the total strain amplitude for the Un-USP and the different USPed conditions. It is evident from **Fig. 5.16b** that at $\Delta\varepsilon_t/2 = \pm$ 0.4% there is a significant increase in N_i whereas, at the highest $\Delta\varepsilon_t/2$ (± 0.8%), there is a drastic reduction in N_i following USP. It may be noted that the scale on X-axis is logarithmic.

5.7.4. Fracture Behavior

Fracture characteristics of the fatigue-tested samples was analyzed by SEM and the fractographs are shown in **Fig. 5.17**. The circles and arrows indicate the sites of the crack initiation and the direction of crack propagation, respectively. Fatigue cracks may be seen initiating from the surface and propagating towards the interior. Fatigue striations are seen clearly in these fractographs.

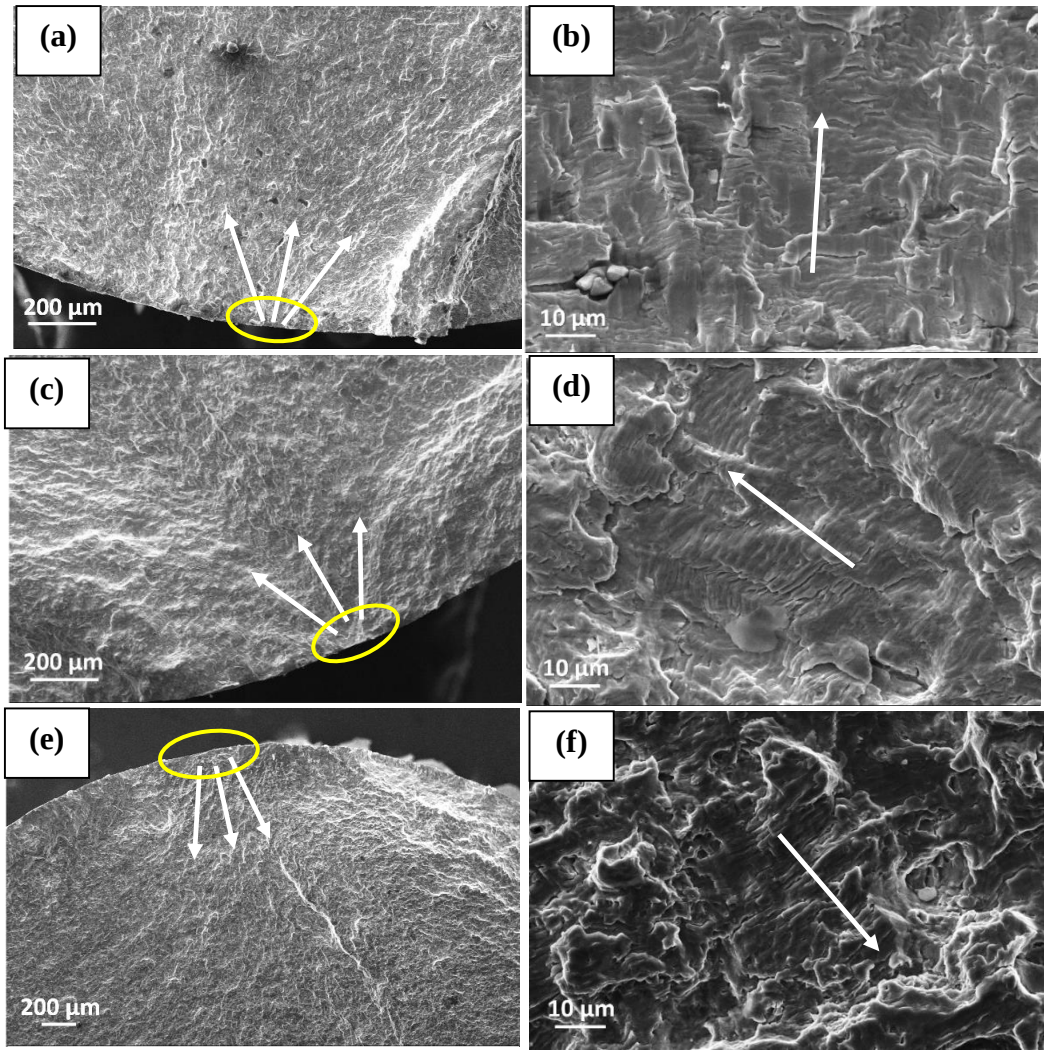

Fig. 5.17. Fracture behavior of the different samples at the total strain amplitude of ± 0.40%: (a, b) Un-USP; (c, d) USP 3-6; (e, f) USP 3-14. Boxes and circles show the crack initiation sites. Arrows indicate the direction of crack propagation.

Fig. 5.18 shows the features on the circumferential regions of gauge sections of the tested specimens, close to the fracture ends. The arrows in these fractographs show the direction of loading and unloading during testing. Most of the cracks were found to form along the bands on the surface. At $\Delta\varepsilon_t/2 = \pm 0.40\%$ very fine micro-cracks were seen (**Fig. 5.18 a, b, c**) whereas at $\Delta\varepsilon_t/2 = \pm 0.80\%$, several cracks were present (**Fig. 5.18 d, e, f**). The density and size (length and width) of cracks are higher for the $\Delta\varepsilon_t/2 = \pm 0.80\%$. The Length, width and density of cracks in the Un-USP condition are higher than that in the USPed condition for the $\Delta\varepsilon_t/2 = \pm 0.40\%$. At $\Delta\varepsilon_t/2 = \pm 0.80\%$, the size and number of

cracks increased with the USP duration which is just opposite to that observed at the $\Delta\varepsilon_t/2 = \pm 0.40\%$, in which the number and size of cracks reduced with increase in the duration of USP.

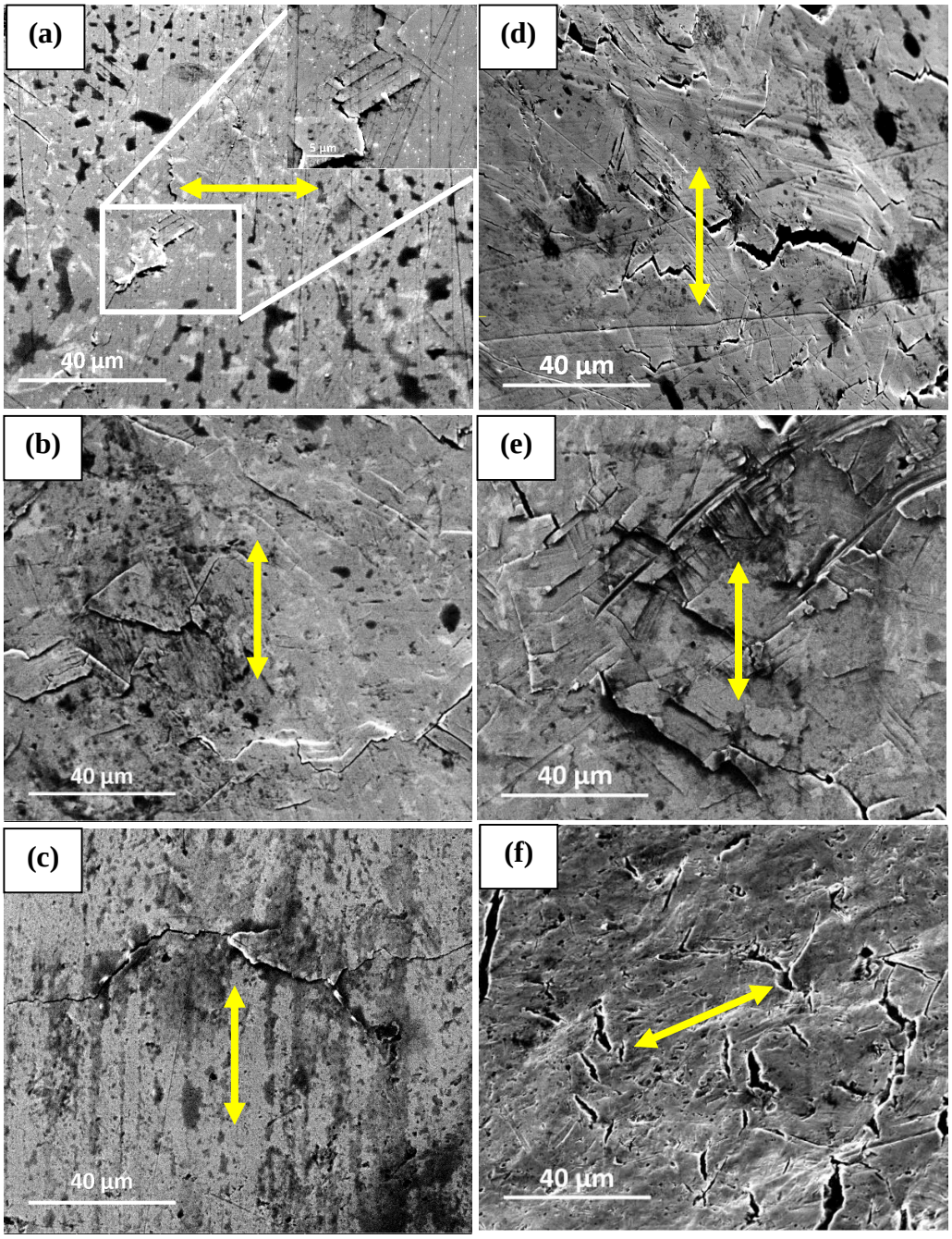

Fig. 5.18. SEM micrographs showing surface morphology of the LCF samples on the periphery (close to fracture ends) of the different samples tested at: (A) $\Delta\varepsilon_t/2 = \pm 0.40\%$: (a) Un-USP, (b) USP 3-3, and (c) USP 3-14; (B) $\Delta\varepsilon_t/2 = \pm 0.80\%$: (d) Un-USP, (e) USP 3-3, and (f) USP 3-14. Arrows indicate the direction of loading.

5.8. Discussion

5.8.1. Surface Nanostructuring by Ultrasonic Shot Peening

Ultrasonic shot peening (USP) of the HNS caused severe plastic deformation in the surface region, as a large number of intersecting twins developed (**Fig. 5.3**). Various polygon structures are present near the USPed surface, which is attributed to extensive intersections of multiple twins in the surface region. The twins' intersection may be seen in TEM micrographs of the USPed samples at a depth of ~ 20 μm from the treated surface. This twinning is attributed to a very high strain and strain rate at a very high frequency of 20 kHz during USP in the surface region. As the distance from the USPed surface towards the interior increased, the induced strain and the severity of deformation decreased, in line with the earlier observation [189]. The increase in the USP-affected region may be seen with the shot size due to the higher energy associated with bigger shots. The depth of the microstructural modification depends on the energy associated with impacting shots; with increase in the induced energy, the effect of USP increases. Since there is little difference in the velocity transferred to shots of 2 mm and 3 mm diameter by the sonotrode, the kinetic energy associated with bigger shots was more because of their larger mass [190]. Thus, bigger size of shots caused refinement to a larger depth.

X-ray peak broadening due to the USP is evident from **Fig. 5.4**. Quantitative analysis of peak broadening shows grain refinement to ~12 nm in the USP affected region of the specimen, subjected to 14 minutes of USP with 3 mm shots. Apart from that of the austenite matrix in the USPed samples, the absence of any other peak shows that no phase transformation occurred in the HNS due to the USP. Deformation-induced martensitic transformation has been reported in conventional austenitic stainless steels, from extensive plastic deformation in the surface region from the surface modification

treatments like SMAT and SMRT [141,158,169]. In an earlier study by Lee et al. [191], the absence of deformation-induced martensitic transformation was observed in the Fe-18Cr-10Mn-N stainless steel containing 0.51 wt% of N, even after straining to 40% true strain. Sjoberg [78] proposed an equation to estimate the effect of N and other alloying elements on the M_{d30} temperature, as given in **Eq. 1.2**. According to **Eq. 1.2**, M_{d30} temperature is ~ -460 ºC for the present composition, which is much lower than that estimated for the Fe-18Cr-10Mn-N alloy with 0.51 wt% of N (-172.60 ºC). The absence of strain-induced martensite in the present investigation, where the contents of N and Mn (the austenite stabilizers) are even higher than that studied by Lee et al. [191], may thus be understood.

XRD and TEM analysis confirmed the formation of nanostructure. Selected area diffraction (SAD) pattern of the USPed samples shows discontinuous rings; thus, refinement of the initial coarse grains into ultrafine grains of nano size with random crystallographic orientations is further confirmed. The clustering of SAD spots in some rings indicates the presence of many nanograins of common crystallographic orientation. Rapid refinement of grains occurs from USP of the FCC materials with low stacking fault energy (SFE). Stacking fault energy (SFE) of the nitrogen stabilized stainless steel is low; it was 41 mJ/m^2 for the Fe-15Cr-17Mn-0.8N and 22.8 mJ/m^2 for the Fe-18Cr-10Mn-0.69N [71,72]. Multiple slip systems are activated at a very high strain rate to accommodate the large strain in the surface region and the extensive intersection of twins occurs. Eventually, the coarse grains get subdivided from the repetitive impacts of shots at high velocity [169,189,192]. Multidirectional twins are expected to orient at ~70.5º, but in the present case, they were oriented at ~72.5º (**Fig. 5.6**) that may be due to high dislocation density at the twin-matrix interface [192]. A slight change occurs in the size of grains from increase in the duration of USP and shot size, and the microstructure in

the USPed surface gets stabilized. The refinement process of grains gradually shifts to consecutive layers, but with decreasing severity of deformation, and the grain size increases. Thus, gradient microstructure develops with a progressive increase in the size of grains from the USPed surface to the substrate.

USP caused enhancement in surface hardness and roughness of the samples is in line with the earlier observations [150,190]. The decrease in plastic deformation with increasing depth from the USPed surface is reflected from the hardness profile (**Fig. 5.8**). Surface undergoes severe plastic deformation and extensive work hardening causes a marked increase in the hardness. The increase in hardness was due to the synergistic effect of the grain refinement and severe strain hardening. Initially, surface roughness was increased significantly following USP (**Table 5.1 and 5.2**). However, with a longer duration of USP, the average roughness decreased. During the USP, dimples like features formed on the USPed surface (**Fig. 5.1**). After a critical duration of USP, new dimples do not form on the surface due to the extensive work hardening [150]. The continuation of peening leads to overlapping of the dimples and causes decrease in the size of dimples (depth and diameter) and surface roughness. Decrease in roughness from longer duration of SMAT was observed in AISI 409 stainless steel with 2 mm shots [193] and in the AISI 304 stainless steel with 2, 5 and 8 mm shots [194]. The plastic deformation caused by bigger shots is more and leads to formation of bigger dimples.

5.8.2. Effect of Ultrasonic Shot Peening on Corrosion Resistance

USP significantly affects the surface condition of the material, which can influence its corrosion resistance. The corrosion potential and corrosion current density of the USP 2-0.5 specimen are comparable to that of the Un-USP specimen. However, the USP 2-1 sample showed better corrosion properties than that of the Un-USP. When the USP was carried out for longer duration, there was decrease in corrosion resistance. Various factors

like microstructural refinement, roughness, compressive residual stress, electron work function (EWF) and surface defects influence the corrosion behavior of materials for a given combination of media and metal. Balusamy et al. [194] have reported negative effect of SMAT on corrosion behavior of 304 SS in 0.6 M NaCl. They observed aggressive corrosion for bigger shots used for SMAT due to increased roughness, martensitic transformation and higher density of dislocations. For 409 SS [193], improved corrosion behavior has been reported after SMAT with 2 mm shots up to 45 minutes and 5 mm shots for 15 minutes, whereas corrosion behavior was found to be deleterious for 8 mm shots. Enhancement in corrosion properties is attributed to grain refinement, whereas increase in microstrain and defect density are attributed to deteriorating effects. Compressive residual stress on the surface enhances the passivation behavior of the stainless steel [195].

In the present study, passivation is found in all the conditions. Nanostructured surface caused by USP has notably high number of grain boundaries which may provide high density of nucleation sites. Initially, there is rapid dissolution of elements, which may lead to formation and presence of very high amount of NH_4^+ which could promote repassivation and inhibit the growth of pits [67]. An increase in the distribution of Cr in the passive film of nanocrystalline material has been reported earlier in the Fe-10 Cr nanocrystalline coating [157] and in the 309 steel [156]. Therefore, nanostructured surface with highly uniform distribution of elements can promote the rapid formation of Cr rich highly protective passive oxide layer on the surface compared to the Un-USP. Further, increase in surface defects increases the preferential sites for corrosion and decreases the electron work function [196], which promote uniform corrosion. Wang and Li [138] found decrease in the electron work function after sandblasting of 304 stainless steel, and increase in it after annealing treatment and consequent enhancement in

corrosion resistance. As seen from Fig. 5.10, there is instantaneous passivation and enhancement in the passivation range of the USP 2-0.5, USP 2-1 and USP 3-0.5 samples. It may be due to the nanostructuring, compressive residual stress and little damage of the surface. However, due to increase in the duration of USP, there is rise in surface defects due to localised erosion and excessive work hardening and the corrosion current density increased as observed earlier [170]. Bigger size shots caused more energy transfer to samples and generated more surface defects compared to smaller size shots. As shown in **Fig. 5.2**, there is erosion of material from longer duration of USP. It causes inhomogeneity on the surface and gives rise to pit-like features (**Fig. 5.2 c, e, f**). The concentration of chloride ions becomes more in such regions than that in the smooth region and concentration cells develop, increasing the corrosion rate and passive current density. All the USPed samples, except the USP 2-0.5, USP 2-1 and USP 3-0.5, showed higher passive current density than that of the Un-USP, which may be due to the defective character of the passive layer formed on those USPed samples; thus, it is attributed to imperfect surface.

5.8.3. Effect of Ultrasonic Shot Peening on *in vitro* Cell Culture and Proliferation

Cell adhesion and proliferation on materials are affected by the chemical and physical nature of the material surface, on which cells are supposed to interact [131]. As shown in **Figs. 5.11 and 5.12**, it can be concluded that the USP does not inhibit cell proliferation; rather, it enhances up to some extent. Due to nanoscale refinement of grains caused by the USP, the significant increase in the grain boundaries may act as preferential sites for the adsorption of proteins to the surface of the implant material [197]. Higher protein adsorption significantly increases the biological function of cells at the interface of tissue-implant [197,198]. Enhancement in hydrophilic nature of material, after severe shot peening was also observed earlier [150,151]. The hydrophilicity/wettability is affected

by both surface topography and nanostructure, as established by Bagherifard et al. [199]. In the surface region, the material gets refined to nanoscale even after 30 seconds of USP. The successive increase in duration of USP and shot size contribute to very little change in the surface characteristics, which may not be significant for further enhancement in the cell response. Residual stress had a significant effect on cell adhesion. Lee et al. found significantly low number of cells in the region of high compressive stress and concluded that cells changed their distribution, without changing morphology, on compressive strained substrate [200]. The residual compressive stress increased with increase in the duration of USP. On the other hand, there was decrease in grain size in nanoscale regime, with increasing duration of USP. Therefore, there was no observable adverse effect of the residual stress on cell proliferation.

5.8.4. Effect of Ultrasonic Shot Peening on Low Cycle Fatigue Behavior

The variation of the cyclic stress amplitude, with the number of cycles at $\Delta\varepsilon_t/2$ from ± 0.40% to ± 0.80% in the present investigation, is similar to that in the earlier study on the HNS [167]. The increase in the cyclic stress in the USPed conditions compared to that of the Un-USP may be attributed to the synergistic effect of the work hardening and nanostructure in the surface region [144,158]. Fatigue life of the HNS in the various conditions is analyzed using the strain-life relationship. The values of the different fatigue parameters (ε'_f & c) are presented in **Table 5.6**. Fatigue life is affected by surface nanostructure, ductility and associated residual stress. The increase in the LCF life following USP, especially at the lower strain amplitudes, can be understood in terms of nanostructuring at the surface and the associated residual compressive stress in the surface region (**Fig. 5.9**).

At $\Delta\varepsilon_t/2 = \pm 0.40\%$; there is a significant difference in the variation of $|\sigma_t|$-$|\sigma_c|$ between the Un-USP and USPed samples, whereas at $\Delta\varepsilon_t/2 = \pm 0.80\%$ this difference is

insignificant **(Fig. 5.14)**. **Fig. 5.14a** shows that the compressive stress at $\Delta\varepsilon_t/2 = \pm 0.40\%$ is higher than that of the tensile stress for the USPed samples, and $|\sigma_c|$ remains higher till the initiation of macro-crack. This observation is in line with the earlier investigation on the microalloyed steel in which the residual compressive stress induced by shot peening relaxed after a few initial cycles at higher strain amplitude, and the relaxation decreased with decrease in the total strain amplitude [201,202]. The compressive residual stresses exert a positive effect on fatigue life [203]. The nanostructured surface layer and gradually increasing grain size from the USPed surface to substrate, associated with compressive residual stress, retard the crack propagation rate as shown in the fractographs in **Fig. 5.17**. Further, number density of striations is increased with increase in the duration of USP. Thus, the crack propagation rate in the USP-affected region is slower than that in the Un-USP samples. The significant enhancement in fatigue life at the lowest $\Delta\varepsilon_t/2 = \pm 0.4\%$ may be analyzed from **Fig. 5.16b** which shows the variation of the two parts of the fatigue life: one showing the cycles spent in the process of macro-crack initiation (N_i), and the other showing cycles spent in crack propagation (N_p). It may be seen from **Fig. 5.16b** that for all the conditions (Un-USP and various USPed), there is little difference in N_p; whereas, there is a marked increase in N_i with the duration of USP. Thus, enhancement of fatigue life at the lower strain amplitude is primarily due to high resistance of the material against crack initiation. Furthermore, a large number of grain boundaries in the nanostructured material reduce dislocation gliding and slip band formation and eventually resist fatigue crack initiation [158]. No change in the microstructure in the ultrafine grain region was observed even after fatigue testing at $\Delta\varepsilon_t/2 \pm 0.50\%$ [204]. Also, as shown in **Fig. 5.18**, it is clear that the number density of cracks on the surface of the samples treated by USP decreases with increase in the duration of USP. Further, surface roughness is deleterious to fatigue resistance of

materials [205]. At the lower $\Delta\varepsilon_t/2$, the positive role of residual compressive stress dominates over the negative effect of roughness and decrease in ductility. Eventually, fatigue life increases significantly.

At high strain amplitudes, compressive residual stress relaxes within a few cycles in the beginning. The USP affected layer also increases in thickness with the USP duration and ductility of the affected region falls with the USP duration. In general, materials fail when the plastic strain accumulating with each cycle reaches a threshold value (ductility exhaustion theory). At higher $\Delta\varepsilon_t/2$, plastic strain is higher, which can cause early ductility exhaustion. With increase in the duration of USP, there is decrease in the global fatigue ductility of material as evident by reduction in the fatigue ductility coefficient (ε'_f) (**Table 5.6**). Also, a significant reduction in ductility from 55 % to ~ 3.4% has been reported for stainless steel following nanocrystallization [144]. Therefore, in the absence of residual stress after a few initial cycles at $\Delta\varepsilon_t/2 = \pm 0.80\%$, cracks usually initiated from the strong USP-affected region and there is a fall in fatigue life. At higher $\Delta\varepsilon_t/2$ ($\pm 0.80\%$), there is reduction in fatigue life, following the USP treatment, in line with the earlier observation made in the 316L stainless steel at $\Delta\varepsilon_t/2 = \pm 1.25\%$ [165].

The significant enhancement in cyclic life of the HNS from the USP, nearly by 18 times in this investigation, is in sharp contrast, with that reported by Rai et al. [167], where USP was carried out with 3 mm shots for 10 minutes and fatigue tests were conducted at higher total strain amplitudes of ±0.60%, ±0.80% and ±1.0% and fatigue life was reduced. It is essential to point out that there was reduction in cyclic life at the higher strain amplitudes of ±0.60% and ±0.80% after 10 minutes of USP, with the same size of shots (3 mm), is in line with the earlier observations [167]. However, a marked increase in the fatigue life was noted at the lower strain amplitudes ($\Delta\varepsilon_t/2 \leq 0.50\%$).

5.9. Conclusions

The effect of USP on microstructure, surface morphology, hardness, corrosion behavior, cell culture and proliferation, and low cycle fatigue of the HNS was evaluated. The microstructure near the USPed surface got modified following the USP. The USP affected layer was found up to the depth of ~ 140 μm, ~ 150 μm, ~ 260 μm and ~ 300 μm resulting from USP 2-1, USP 3-1, USP 3-3 and USP 3-6, respectively. There was an increase in the USP affected layer with an increase in shot size and duration of USP. The initial coarse-grained microstructure of the HNS was refined to nanoscale, following USP. Nanograins of 22 nm and 20 nm were produced by USP for 30 s with shots of 2 mm and 3 mm diameter, respectively and it was refined to 12 nm, following 14 min of USP with 3 mm shots. There was a gradual change in microstructure from USPed surface to interior. Nanograined structure was found just near the surface and there was a progressive change in the microstructure, from multidirectional twins to single direction, which ultimately disappears, from the USPed surface towards interior, up to a certain depth, depending on the shot diameter and the duration of USP. No phase transformation was observed even after 14 min of USP with 3 mm diameter shots. There was increase in the hardness following USP. It was found to increase by 42% at the surface by 2 minutes of USP with 3 mm shots and was reduced gradually from surface towards interior.

Corrosion resistance of the HNS in SBF was increased following USP for shorter duration, whereas it was reduced from longer durations of USP due to excessive surface damage. Thus, it is evident that the corrosion resistance of the HNS varied with the USP treatment, in terms of the shot size and the duration of peening. The USP affects important factors like surface roughness, defect density and microstructural refinement which play important role on corrosion behavior. This study shows that it is essential to

optimize the USP for the enhancement of corrosion resistance. For the HNS, 30 seconds and 1 minute of USP with shots of 3 mm and 2 mm diameters, respectively, are the optimum conditions in terms of peening duration and diameter of shots for enhancement of corrosion resistance. Surface modification by USP of the newly developed stainless steel did not inhibit cell proliferation; instead, it improved up to some extent. Statistical analysis showed that the difference in cell proliferation for different time points was significant at the level of 0.05.

There is a continuous decrease in the LCF life of the USPed samples with the duration of USP at the highest strain amplitude of ± 0.80%; however, there is a marked increase in fatigue life at the lowest strain amplitude of ± 0.40%. The fatigue life was increased by ~ 18 times at $\Delta\varepsilon_t/2 = \pm 0.40\%$, by the USP with 3 mm shots for 18 min. The marked enhancement in the LCF life from USP at the lowest strain amplitude was mainly due to the delay in the process of crack initiation, from the nanostructured surface and the associated compressive residual stress. Thus, it is evident that for a given shot diameter and vibrating amplitude at a constant frequency, the optimum duration of USP must be determined to avoid surface damage from excessive USP and it must be realized that the effect of USP on fatigue life is highly dependent on the applied strain amplitude.